



Cite this: *RSC Adv.*, 2025, 15, 50324

Strategic advances in defect-engineered Ce–Bi₃YO₆/rGO hybrids for rapid crystal violet mineralization under visible illumination

Muhammad Shahid,^a M. M. Rashed,^b Mohamed Abdel Rafea,^b Mohamed Ibrahim Attia,^c Mohamed R. El-Aassar,^d Abdullah K. Alanazi,^e Imran Shakir,^f Muhammad Aadil *^g and Mazen R. Alrahili^h

Systemically tailored cerium-doped Bi₃YO₆/rGO ceramic nanohybrids were prepared by a sequential hydrothermal-ultrasonication approach to surmount the innate limitations of binary metal oxides in visible-light photocatalysis, such as limited spectral absorption and fast electron–hole recombination. Incorporation of rare earths (Ce³⁺/Ce⁴⁺) into the Bi₃YO₆ lattice introduces defect-assisted carrier trapping and local band structure reconfiguration, while conductive wrapping with rGO forms an interconnected network of charge transport, enabling spatial electron migration and thus recombination suppression. Comprehensive physicochemical characterization by XRD, FTIR, TGA, and SEM; optical studies (UV-vis, PL); and electrical/electrochemical analyses (*I*–*V*, EIS, transient photocurrent) evidenced crystalline cubic Bi₃YO₆ with a flake-like morphology, a narrowed bandgap from 2.74 to 2.56 eV, superior light harvesting capability, and reduced interfacial resistance in the hybrid photocatalyst compared with its pristine counterpart. Under visible-light irradiation ($\lambda > 420$ nm), the optimized Ce–Bi₃YO₆/rGO displayed excellent photocatalytic activity toward crystal violet degradation, yielding 92.04% removal ($k = 0.0800$ min^{−1}), significantly higher than those of Ce–Bi₃YO₆ (76.28%) and Bi₃YO₆ (62.37%). Scavenger experiments confirmed that [•]OH and [•]O₂[−] species dominated the oxidative pathways, further confirming the proposed radical-driven mechanism facilitated by rGO-directed electron extraction. The catalyst showed strong reusability, with efficiency retention of >84% after five cycles, thus confirming outstanding structural robustness and photochemical durability. This work develops a synergistic approach that involves defect engineering and carbon-framework incorporation to further advance Bi-based ceramic photocatalysts toward a scalable and high-performance platform for visible-light-driven wastewater remediation.

Received 5th November 2025
Accepted 9th December 2025

DOI: 10.1039/d5ra08524a

rsc.li/rsc-advances

1. Introduction

Inspired by the process of photosynthesis in nature, solar-light-mediated photocatalysis—a cost-effective, sustainable, and

facile technique—has been developed for rapidly addressing global environmental and water pollution issues.^{1,2} Unlike conventional remediation methods, photocatalysis utilizes a clean and abundant energy source (solar light).^{3–5} Despite its compelling potential, photocatalysis has not yet been recognized for industrial adoption due to several key challenges, including limited visible-light absorption, photogenerated hole–electron pair recombination, and photocorrosion of the photocatalyst.⁶ For instance, the extensively investigated photocatalyst titanium oxide TiO₂ exhibits a wide bandgap *E*_g and responds to ultraviolet light, which contributes to a minor extent in the solar spectrum.^{7,8} The practical implementation of photocatalysis requires rationally designed photocatalysts with substantial quantum efficiency.

In the relentless pursuit of photocatalytic materials with high photocatalytic efficacy, a vast collection of semiconductor single metal oxides, CuO,⁹ ZnO,¹⁰ WO₃,¹¹ Fe₂O₃,¹² SnO₂,¹³ In₂O₃,¹⁴ CeO₂,¹⁵ NiO,¹⁶ TiO₂,¹⁷ and binary metal oxides, NiCo₂O₄,¹⁸ SrFe₁₂O₁₉,¹⁹ NiFe₂O₄,²⁰ Ni₃V₂O₈,²¹ has been

^aDepartment of Chemistry, College of Science, University of Hafr Al Batin, P.O. Box 1803, Hafr Al Batin 31991, Saudi Arabia

^bDepartment of Physics, College of Science, Imam Mohammad Ibn Saud Islamic University (IMSIU), 11623 Riyadh, Saudi Arabia

^cDepartment of Chemistry, College of Science, Imam Mohammad Ibn Saud Islamic University (IMSIU), 11623 Riyadh, Saudi Arabia

^dDepartment of Chemistry, College of Science, Jouf University, PO Box 2014, Sakaka, Aljouf, Saudi Arabia

^eDepartment of Chemistry, College of Science, Taif University, Taif, Saudi Arabia

^fDepartment of Physics, Faculty of Science, Islamic University of Madinah, Madinah, 42351, Saudi Arabia

^gDepartment of Chemistry, Rahim Yar Khan Campus, The Islamia University of Bahawalpur, Rahim Yar Khan, 64200, Pakistan. E-mail: muhammad.aadil@iub.edu.pk

^hDepartment of Physics, College of Science, Taibah University, Madinah, Saudi Arabia



investigated to remove the obstacles in leveraging photocatalysis for practical application, but the intrinsic (pure) materials suffer from the typical challenges, dropping the quantum efficiency.²² Binary metal oxides, for instance, bismuth yttrium oxide (Bi_3YO_6), have low photoresponse and sluggish electron-hole transport for the redox reaction, which notably controls their photocatalytic efficacy.^{23,24} Different modification strategies, specifically metal doping and composite designing with a conductive framework like rGO, have given promising results to extend the visible-light photo-response, reducing the electron-hole recombination.^{25–27} The extended π -conjugation, in addition to conductive pathways, assists the spatial transfer of electrons from the semiconductor to the rGO, physically separating the electron-hole driving availability for the redox reaction.²⁸ Despite the significant development of rGO-based photocatalysts and metal-doped bismuth oxides, Ce-doped Bi_3YO_6 remains almost unexplored in the literature, and no previous report has demonstrated its visible-light-driven photocatalytic behavior. No study has been conducted on the construction of a Ce- Bi_3YO_6 /rGO hybrid heterojunction to date, and the synergistic role of $\text{Ce}^{3+}/\text{Ce}^{4+}$ defect levels with a conductive rGO framework remains unreported. Besides, there has not been any previous report of Bi_3YO_6 -based photocatalysts concerning the degradation of crystal violet, hence a clear application gap. Thus, this work bridges an important gap by proposing a novel defect-engineered Bi_3YO_6 system integrated with rGO that overcomes recombination losses to extend the visible-light activity.

In this work, a rationally engineered cerium-doped Bi_3YO_6 material integrated with rGO as an efficient Ce- Bi_3YO_6 /rGO hybrid has been prepared to address the issues of limited visible-light activity and fast charge recombination associated with conventional photocatalysts. Accordingly, Bi_3YO_6 and Ce- Bi_3YO_6 were synthesized by a simple hydrothermal method and then treated by ultrasonication to uniformly encapsulate Ce- Bi_3YO_6 within rGO sheets. The synthesized materials were examined through a range of structural, optical, electrical, and electrochemical techniques to gain a clearer picture of their phase evolution, surface morphology, and charge-transport characteristics. Photocatalytic activity was studied by following the breakdown of crystal violet under visible light. The CV degradation kinetics, scavenging studies, and reusability of Ce- Bi_3YO_6 /rGO have been explored to systematically quantify the solar-light-mediated photocatalytic efficacy.

2. Experimental

2.1 Chemicals

The metal precursors, yttrium nitrate hexahydrate ($\text{Y}(\text{NO}_3)_3 \cdot 6\text{H}_2\text{O}$, 99.99%), bismuth nitrate pentahydrate ($\text{Bi}(\text{NO}_3)_3 \cdot 5\text{H}_2\text{O}$, $\geq 99.99\%$) and ceric ammonium nitrate ($(\text{NH}_4)_2[\text{Ce}(\text{NO}_3)_6]$, $\geq 98.5\%$), and reduced graphene oxide (rGO, chemically reduced, powder, ($k > 600 \text{ S m}^{-1}$) were sourced from Sigma-Aldrich, and used for the synthesis of Bi_3YO_6 , Ce- Bi_3YO_6 , and Ce- Bi_3YO_6 /rGO. For the photocatalytic test, crystal violet dye (CV, $\text{C}_{25}\text{H}_{30}\text{N}_3\text{Cl}$, 407.98 g mol^{-1}) was degraded. At the same time, the quenchers, Isopropyl Alcohol (IPA), *p*-benzoquinone (p-BQ), silver nitrate (AgNO_3), and

disodium salt of ethylenediaminetetraacetic acid (EDTA-2Na), were used for the scavenging studies. Deionized water ($k < 6 \mu\text{S cm}^{-1}$) was used for synthesis, washing, and photocatalytic test.

2.2 Fabrication of Bi_3YO_6 , Ce- Bi_3YO_6 , and Ce- Bi_3YO_6 /rGO

The pure Bi_3YO_6 and cerium-doped Ce- Bi_3YO_6 materials were fabricated from the hydrothermal method. The precursor, bismuth nitrate and yttrium nitrate, solutions in stoichiometric (3Bi : 1Y) amounts were dissolved in DI water, and the pH was shifted to an alkaline level (pH ~ 9 –9.5) by the addition of NaOH, with vigorous stirring until the clear solution appeared. The reaction mixture was transferred to the Teflon cup sealed in an autoclave and heated at 200 °C for 12 hours. Once the hydrothermal treatment was completed, the autoclave was set to cool down to room temperature, and the precipitates were collected, washed multiple times to ensure the removal of unreacted precursors, and dried in an oven. The precipitate powder was calcinated to acquire the Bi_3YO_6 phase. A similar procedure was followed to synthesize Ce- Bi_3YO_6 in a stoichiometric amount (0.05Ce : 2.95Bi : 1Y). The Ce- Bi_3YO_6 material was encased in rGO sheets to synthesize the synergistically-modified Ce- Bi_3YO_6 /rGO material by ultrasonication. Initially, 270 mg of the fabricated Ce- Bi_3YO_6 were added to 100 mL DI water and 30 mg of rGO powder in 100 mL DI water in separate beakers and sonicated for 1 hour, followed by their mixing and sonication for 2 hours to evenly encase the Ce- Bi_3YO_6 in rGO covering.

2.3 Characterization

The phase composition, crystal structure, thermal stability, morphology and microstructure, optical, electrical, and electrochemical response were investigated by powder X-ray Diffraction (XRD/ $2\theta = 20$ – 60° /Cu-K α $\lambda = 0.154 \text{ nm}$ /Shimadzu 6100 AS X-ray Diffractometer), Fourier Transform Infrared Spectroscopy (FTIR/wavenumber = 4000–400 cm^{-1} /Shimadzu IRAffinity 1S spectrophotometer), Thermogravimetric Analysis (TGA/T = 25–600 °C/TG8120 Rigaku Thermoplus EVO), Scanning Electron Microscopy (SEM/FEI S50 scanning electron microscope), Transmission electron microscopy (TEM, FEI-CM30 transmission electron microscope), Energy dispersive X-ray spectroscopy (EDS, FEI S50 scanning electron microscope), Photoluminescence spectroscopy (PL/FLS1000 photoluminescence spectrometer), UV-vis spectroscopy ($\lambda = 200$ –800 nm/Jenway 6850 double-beam spectrophotometer), current-voltage analysis (I - V /KEITHLEY/6517B/15 V to +15 V), Electrochemical Impedance Spectroscopy (EIS/IVIUM-n-Stat ZRA Three-electrode potentiostat/1 M Na_2SO_4 Electrolyte), and Transient Photocurrent response ($\lambda > 420 \text{ nm}$ /material pasted ITO substrate).

2.4 Photocatalytic (PC) efficacy studies

The PC efficacy of the Bi_3YO_6 , Ce- Bi_3YO_6 , and Ce- Bi_3YO_6 /rGO was assessed by degrading the CV in aqueous solution under an Xe lamp (equipped with UV cutoff filter) as a visible light source. Typically, in the 100 mL (10 mg L^{-1}) solution of CV, 0.1 g of the catalyst (Bi_3YO_6 /Ce- Bi_3YO_6 /Ce- Bi_3YO_6 /rGO) was dispersed by stirring (30 minutes) in the dark to facilitate the adsorption/desorption equilibria of CV molecules on the surface of the catalyst. The samples at the specified time intervals were



collected from the degradation mixture, and the absorbance was measured. The decrease in CV concentration was measured by applying the relation, $\text{degradation\%} = \left(1 - \frac{A_t}{A_0}\right) \times 100$,²⁹ where A_0 is the initial CV absorbance, and A_t is the absorbance of the sample collected at the specified time interval.

3. Results and discussion

3.1 Structural phase formation and thermal stability

The phase composition and crystal structure phase formation were investigated by powder XRD and FTIR spectroscopy. The precipitates collected from the hydrothermal process were annealed at different temperatures to optimize the annealing temperature for the structural phase appearance of Bi_3YO_6 . The diffraction patterns of the materials annealed at different temperatures ranging from 550 °C to 700 °C with an increment of 50 °C are displayed in Fig. 1(a).

At 700 °C, the Bi_3YO_6 phase appeared and the diffraction peaks at $2\theta = 28.20^\circ$, 32.54° , 46.70° , 55.37° , and 58.01° indexed to (111), (200), (220), (311), and (222) planes and aligns with the standard JCPDS No. 01-079-0390 corresponding to the cubic system with $Fm\bar{3}m$ space group.³⁰ In Fig. 1(b), the overlaid XRD patterns of the Bi_3YO_6 , $\text{Ce-Bi}_3\text{YO}_6$, and $\text{Ce-Bi}_3\text{YO}_6/\text{rGO}$ are presented to distinguish the structural changes after Ce-doping and encasing $\text{Ce-Bi}_3\text{YO}_6$ in rGO covering. No substantial change in the XRD pattern of $\text{Ce-Bi}_3\text{YO}_6$ was observed, but a slight variation in position and a decrease in intensity of diffraction peaks. These changes correspond to crystal lattice alterations by the insertion of cerium ions, but the crystal phase was not destroyed by Ce-doping. For the $\text{Ce-Bi}_3\text{YO}_6/\text{rGO}$ material, the intensity of diffraction peaks was significantly reduced due to rGO covering. The XRD findings indicate Cerium-doping and covering of $\text{Ce-Bi}_3\text{YO}_6$ material with rGO to synergistically-modified $\text{Ce-Bi}_3\text{YO}_6/\text{rGO}$ material.

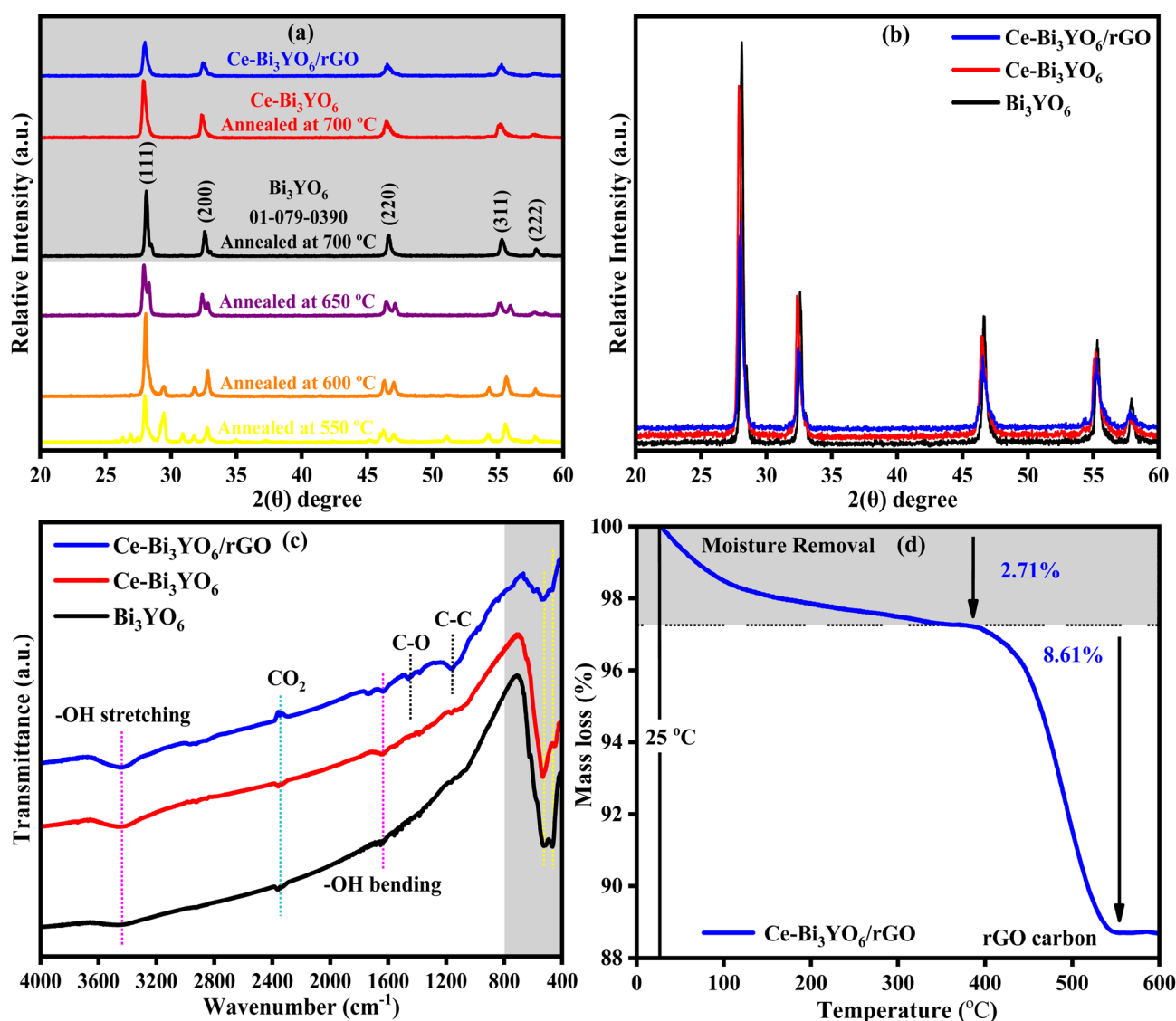


Fig. 1 XRD patterns of the samples annealed at different temperatures (temperature optimization for Bi_3YO_6 phase formation) (a), overlaid XRD patterns (b) and FTIR spectra (c) of Bi_3YO_6 , $\text{Ce-Bi}_3\text{YO}_6$, and $\text{Ce-Bi}_3\text{YO}_6/\text{rGO}$, and TGA profile (d) of $\text{Ce-Bi}_3\text{YO}_6/\text{rGO}$.



The FTIR analysis, spectra are displayed in Fig. 1(c), was performed to confirm the structural phase formation of the synthesized material. The vibrations in the fingerprint region ($<800\text{ cm}^{-1}$) are distinguished as metal–oxygen bond vibrations, M–O ($\sim 526\text{ cm}^{-1}$) and M–O–M ($\sim 464\text{ cm}^{-1}$), where M = Bi/Y, confirming the formation of Bi_3YO_6 materials.³⁰ The additional signatures, which appear for the Ce– $\text{Bi}_3\text{YO}_6/\text{rGO}$, correspond to C–C ($\sim 1163\text{ cm}^{-1}$) and C–O ($\sim 1451\text{ cm}^{-1}$) vibrations, ascribing the rGO covering.^{31,32} The –OH stretching ($\sim 3445\text{ cm}^{-1}$) and bending ($\sim 1636\text{ cm}^{-1}$) are attributed to adsorbed moisture,^{33,34} while the hump around $\sim 2345\text{ cm}^{-1}$ was asymmetric stretching of atmospheric CO_2 .³⁵ The TGA curve of Ce– $\text{Bi}_3\text{YO}_6/\text{rGO}$ ($T = 25\text{--}600^\circ\text{C}$) is presented in Fig. 1(d). The 2.71% mass loss in the lower temperature ($<300^\circ\text{C}$) describes the adsorbed moisture removal, while at the high temperature ($T = 400\text{--}600^\circ\text{C}$), the combustion of rGO carbon reduces 8.61% mass of Ce– $\text{Bi}_3\text{YO}_6/\text{rGO}$.³⁶ Based on the TGA analysis, the Ce– $\text{Bi}_3\text{YO}_6/\text{rGO}$ exhibits thermal stability $<400^\circ\text{C}$.

3.2 Morphological investigation

The morphology and microstructure of the Bi_3YO_6 , Ce– Bi_3YO_6 , and Ce– $\text{Bi}_3\text{YO}_6/\text{rGO}$, materials were explored by the SEM analysis, and the micrographs are presented in Fig. 2. The Ce–

Bi_3YO_6 exhibits a cluster of 2D-like flakes with irregular symmetry and size, which is consistent to the Bi_3YO_6 reflecting Ce-doping has not significantly affected the microstructure and morphology and led to the growth of crystallites as for the Bi_3YO_6 . In the Ce– $\text{Bi}_3\text{YO}_6/\text{rGO}$ material, the thin rGO sheet encases the Ce– Bi_3YO_6 flakes as shown in Fig. 2(c and d). The rGO covering will facilitate spatial charge (photoexcited electron) separation and transport to the conductive 2D conjugated framework of rGO.³⁷

3.3 Hybrid interface and composition

The hybrid interface between the Ce– Bi_3YO_6 and rGO was studied by the TEM investigation, and the findings are presented in Fig. 3(a–c and f). The interface quality significantly controls the rate of photocatalysis, as it mainly drives charge separation and prevents the rapid recombination of the photogenerated charges. The Ce– Bi_3YO_6 exhibits nanoflakes covered with rGO sheets (marked in yellow), forming a high-quality heterojunction that is favorable for charge separation (photo-separated electron transferring) to the rGO conducting channels. The EDS spectrum of the cerium-doped Bi_3YO_6 composition, shown in Fig. 3(d), contains all peaks corresponding to the constituent elements Ce, Bi, Y, and O, ascribing

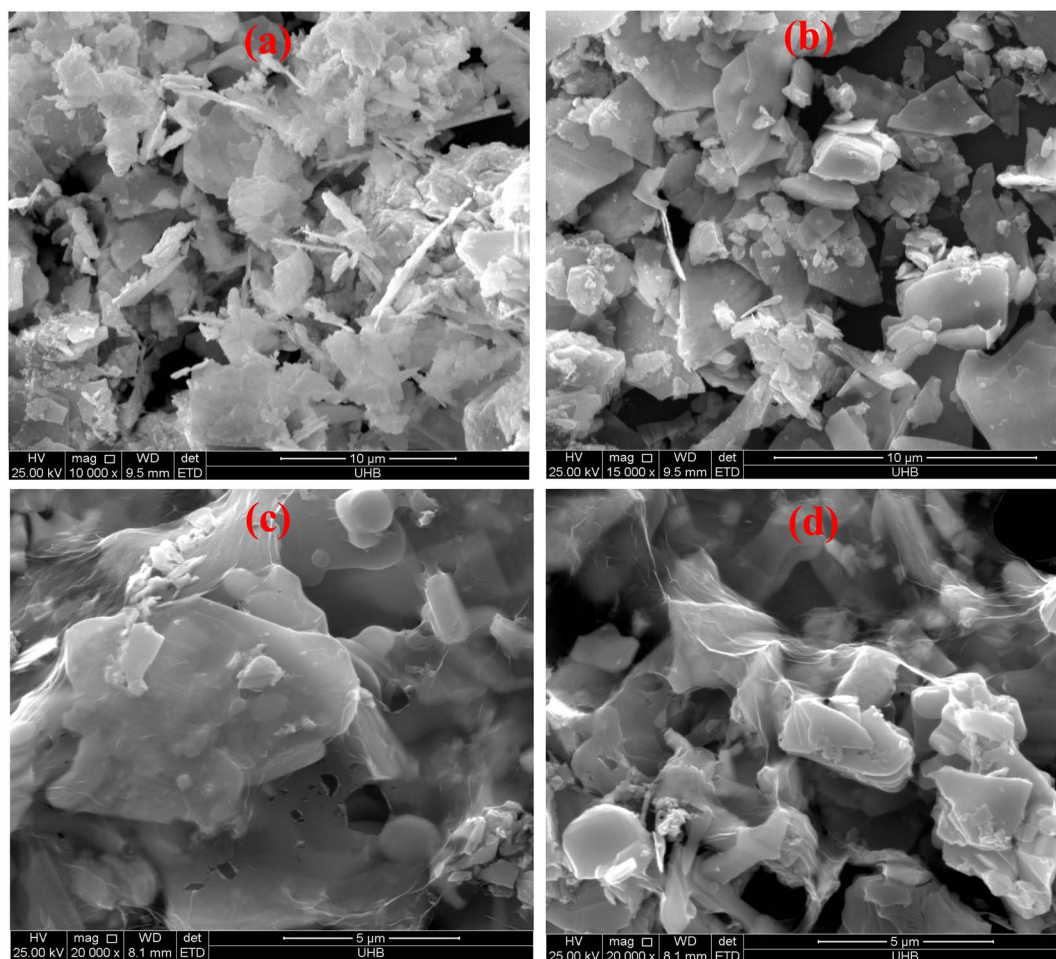


Fig. 2 SEM images of Bi_3YO_6 (a), Ce– Bi_3YO_6 (b), and Ce– $\text{Bi}_3\text{YO}_6/\text{rGO}$ (c and d).

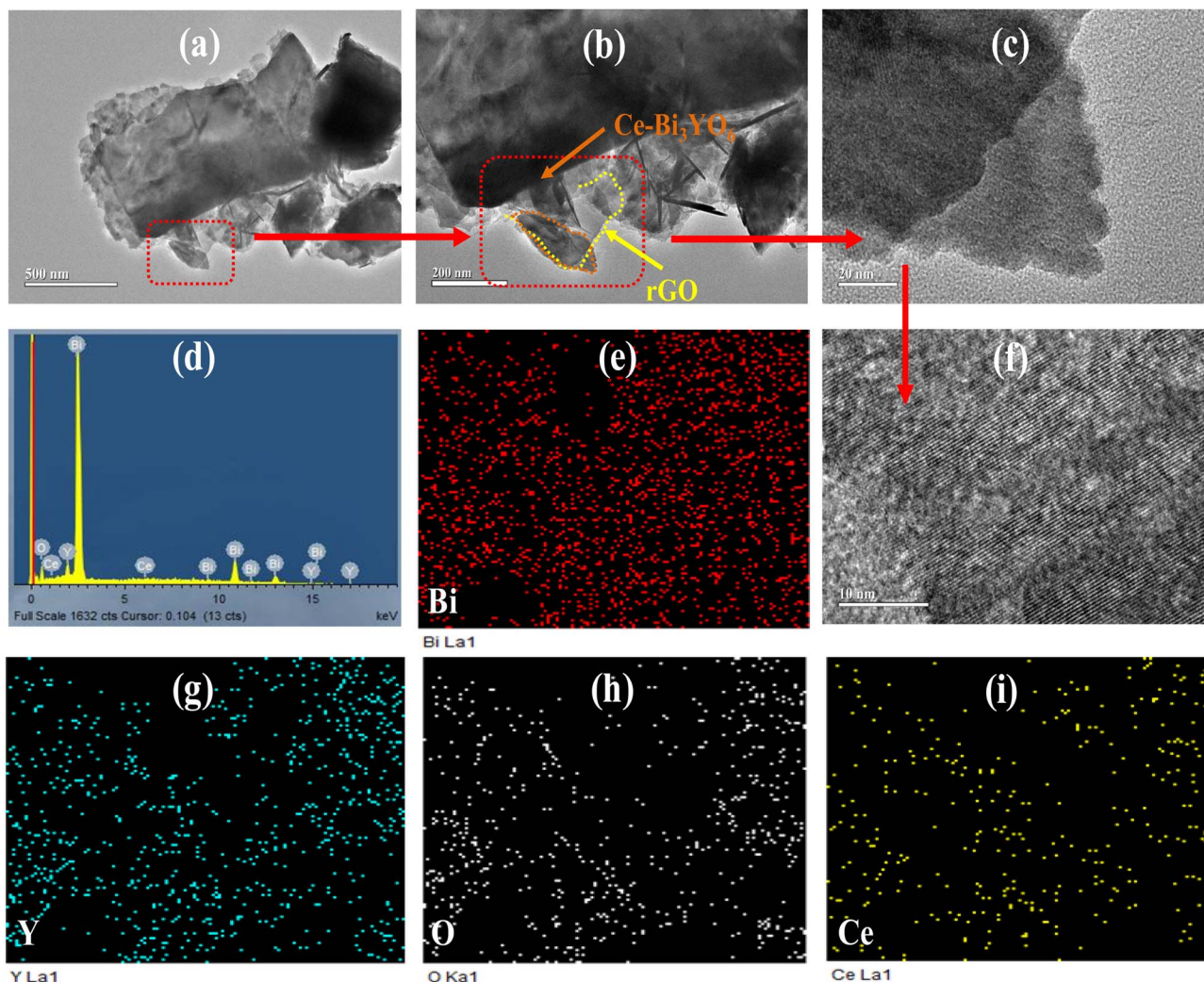


Fig. 3 TEM images of composite Ce-Bi₃YO₆/rGO (a–c, and f) and EDS studies with elemental mapping (d, e and g–i).

the purity of the designed composition, while the elemental mapping is presented in Fig. 3(e and g–i).

3.4 Optical and electrical properties

The solar light-mediated photocatalysis is primarily controlled by the light absorption, which leads to excitation in the semiconductor and separates the charge (h^+/e^-) species. The optical response of Bi₃YO₆, Ce-Bi₃YO₆, and Ce-Bi₃YO₆/rGO was analyzed by applying the UV-vis absorption and photoluminescence (PL) spectroscopy, and the results are presented in Fig. 4(a and b). From the UV-vis spectra, it is clearly evident that the fabricated materials show absorption in the visible light region Fig. 4(b), and the response was extended by modifying the Bi₃YO₆ with Ce-doping and encasing Ce-Bi₃YO₆ with rGO covering, which is promising for solar light (~43% of visible light) mediated photocatalytic applications.³⁸ The bandgap (E_g) was estimated from the UV-vis absorption data by applying the Tauc plot equation,³⁹ as shown in Fig. 4(c). The calculated E_g of Bi₃YO₆, Ce-Bi₃YO₆, and Ce-Bi₃YO₆/rGO were correspondingly 2.74 eV, 2.66 eV, and 2.56 eV. The E_g was narrowed by the Ce-doping and encasing Ce-Bi₃YO₆

into rGO due to the red shift in the absorption edge, which reflects the formation of localized states within the electronic band by incorporation of Ce ions, and development of additional electronic states by rGO, promoting the enhanced visible light absorption.⁴⁰

The impact of synergistic modification, Ce-doping, and rGO encasing on the charge carrier's dynamics was assessed by PL spectroscopy, and the PL response is presented in Fig. 4(a). The unmodified material Bi₃YO₆ shows prominent PL emission in contrast to the Ce-Bi₃YO₆ and Ce-Bi₃YO₆/rGO, which characteristically feature the rapid h^+/e^- recombination.⁴¹ The variable oxidation state of cerium (Ce^{3+}/Ce^{4+}) traps the electrons and delays the rapid h^+/e^- recombination in Ce-Bi₃YO₆, as evident from its PL response.⁴² The substantially quenched PL emission of Ce-Bi₃YO₆/rGO indicates facilitated charge separation, which was due to the rGO encasing. The highly conductive pathways in the rGO framework spatially separate the electrons from the Ce-Bi₃YO₆ and increase their availability for the redox reaction, which directly controls the photocatalytic performance.⁴³ The charge separation and transportation were further validated by the current-voltage (I - V) analysis, and the I - V profiles of the



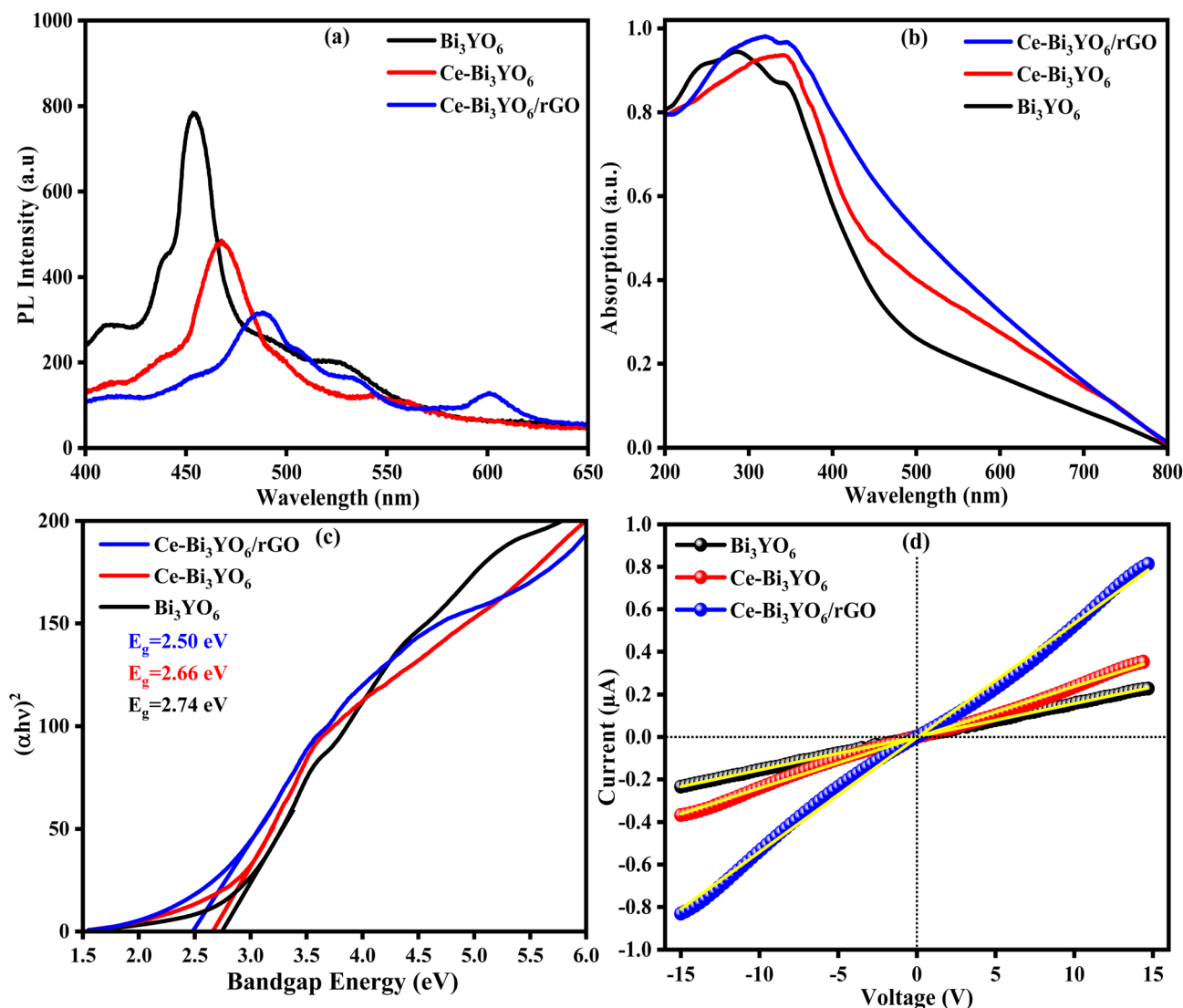


Fig. 4 PL spectra (a), UV-vis absorption spectra (b), Tauc plot fitting (c), and IV profile (d) of Bi_3YO_6 , $\text{Ce-Bi}_3\text{YO}_6$, and $\text{Ce-Bi}_3\text{YO}_6/\text{rGO}$.

Bi_3YO_6 , $\text{Ce-Bi}_3\text{YO}_6$, and $\text{Ce-Bi}_3\text{YO}_6/\text{rGO}$ are presented in Fig. 4(d). Against the applied voltage (-15 V to $+15$ V), the maximum current response was observed for the synergistically-modified $\text{Ce-Bi}_3\text{YO}_6/\text{rGO}$ material,⁴⁴ which reflects the facilitated charge separation and is in accordance with the PL results.

3.5 Electrochemical response

Electrochemical impedance spectroscopy (EIS) and transient photocurrent (TPC) were applied to the fabricated Bi_3YO_6 , $\text{Ce-Bi}_3\text{YO}_6$, and $\text{Ce-Bi}_3\text{YO}_6/\text{rGO}$ materials to analyze the charge carrier dynamics, and the results are presented in Fig. 5(a and b).

The semicircle in the Nyquist plot, which is directly related to the electrode/electrolyte interfacial charge transfer resistance (R_{ct}) and corresponds to the impedance to transfer the photogenerated electrons.^{45,46} The larger-sized semicircle (in the Nyquist plot) of Bi_3YO_6 decreases by Ce-doping and concurrently by rGO encasing Fig. 5(a), which ascribes to reduced R_{ct} by the synergistic modification.⁴⁷ The TPC response was recorded by falling visible

light ($\lambda > 420$ nm) on the material-coated electrode. In Fig. 5(b), the recorded photocurrent density is displayed, which is considerably high for the $\text{Ce-Bi}_3\text{YO}_6/\text{rGO}$ material. The substantial increase in TPC corresponds to the transfer of (photogenerated) electrons to the electrode instead of recombining with the positive holes (h^+), which indicates suppression in h^+/e^- recombination.⁴⁸ The EIS and TPC results, in parallel with the PL emission, describe the facilitated charge separation and transportation in the synergistically modified $\text{Ce-Bi}_3\text{YO}_6/\text{rGO}$ material, rendering a promising photocatalytic efficacy.

3.6 CV degradation

The PC efficacy of the as-synthesized Bi_3YO_6 , $\text{Ce-Bi}_3\text{YO}_6$, and $\text{Ce-Bi}_3\text{YO}_6/\text{rGO}$ catalysts was assessed by degrading CV under visible-light irradiation. The change in CV concentration at the specific time intervals was monitored by recording the absorption spectra, which are presented in Fig. 6. The absorption intensity decline at λ_{max} expresses the decrease in CV

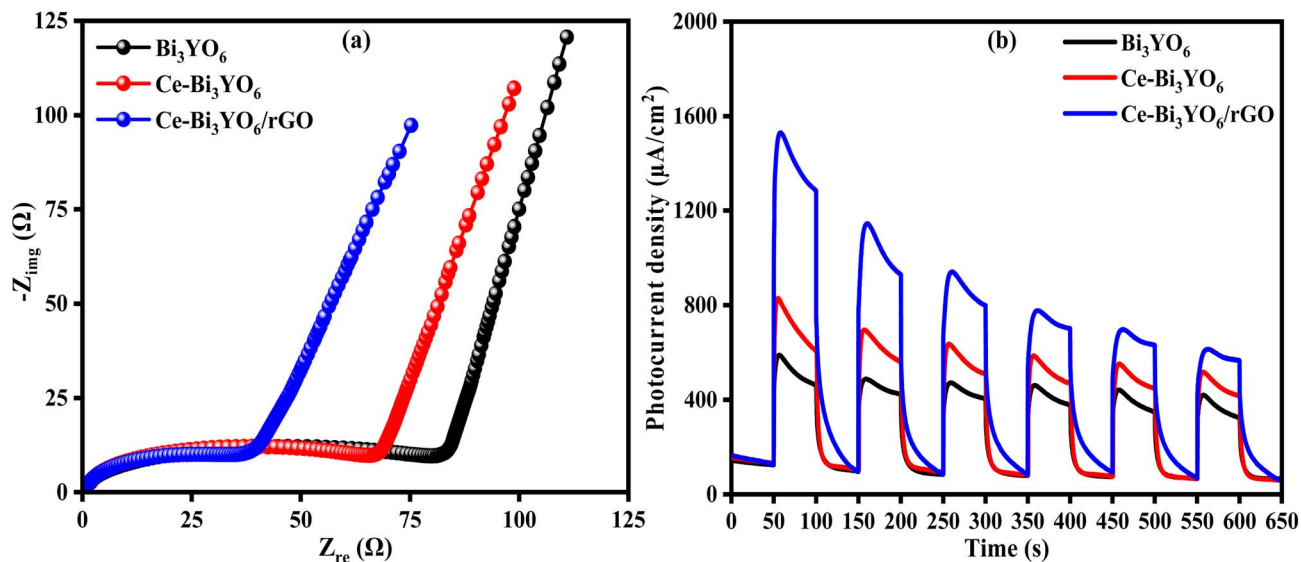


Fig. 5 EIS Nyquist plots (a) and transient photocurrent curves (b) of Bi_3YO_6 , $\text{Ce-Bi}_3\text{YO}_6$, and $\text{Ce-Bi}_3\text{YO}_6/\text{rGO}$.

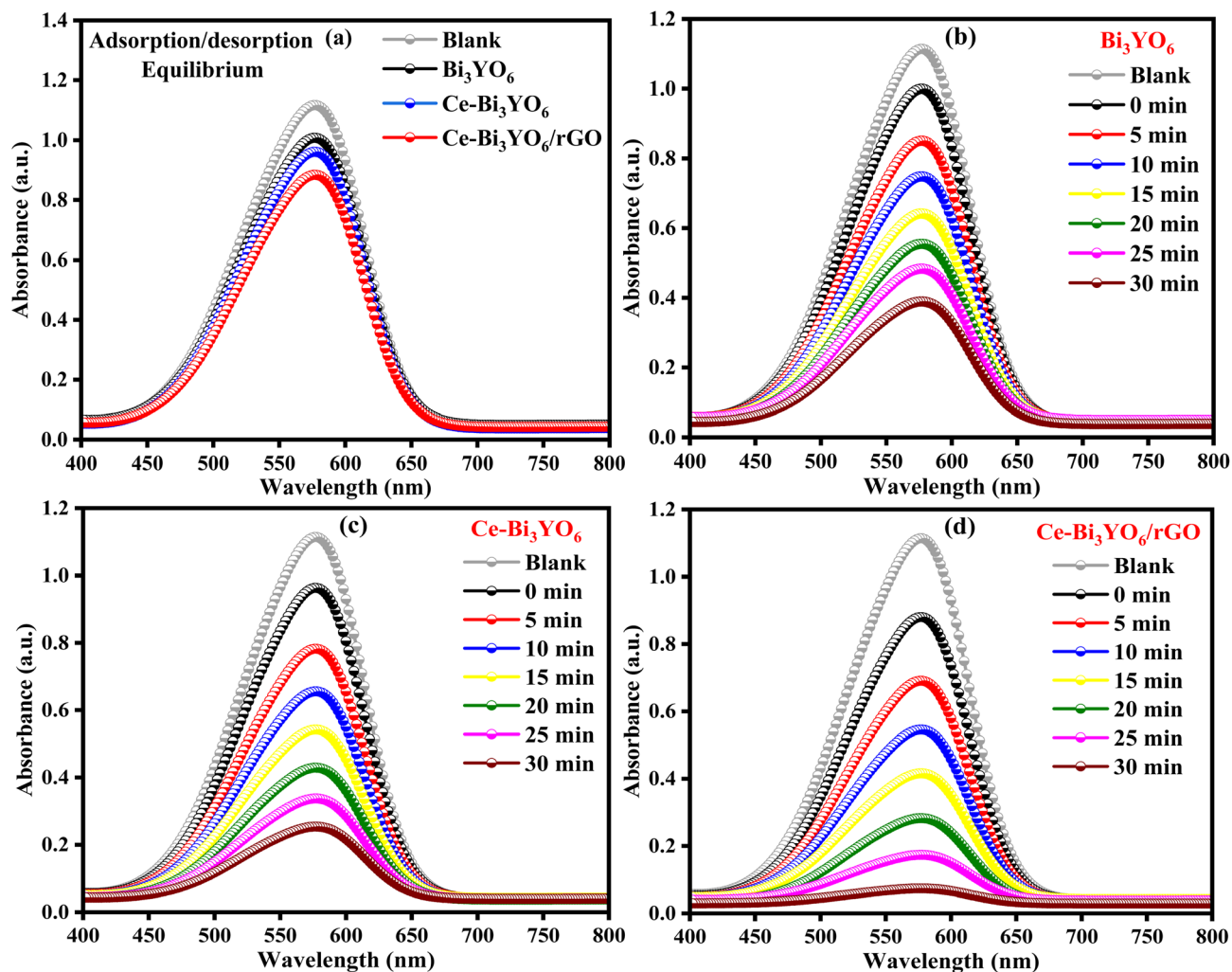


Fig. 6 Adsorption-desorption of CV on the catalysts Bi_3YO_6 , $\text{Ce-Bi}_3\text{YO}_6$, and $\text{Ce-Bi}_3\text{YO}_6/\text{rGO}$ (a), decline in CV concentration by degradation over the Bi_3YO_6 (b), $\text{Ce-Bi}_3\text{YO}_6$ (c), and $\text{Ce-Bi}_3\text{YO}_6/\text{rGO}$ (d).



concentration over time, which is maximum in the presence of the catalyst Ce-Bi₃YO₆/rGO. Notably, the Ce-Bi₃YO₆/rGO displayed the highest photocatalytic efficacy as compared to Ce-Bi₃YO₆ and Bi₃YO₆. Mechanistically, the cerium-doping modifies the Bi₃YO₆ crystal structure and specifically increases the optical response by bandgap tuning, facilitating charge (electron-hole) carrier separation. The encapsulation of Ce-Bi₃YO₆ in rGO enhances the charge separation by spatial transfer of the photoseparated electrons to the conductive channel of the rGO framework.⁴⁹

The degradation over Ce-Bi₃YO₆/rGO was investigated by varying the pH of the working media, the CV concentration, the catalyst dose, and the coexistence of common ions. As presented in Fig. 7(a), the maximum extent in CV degradation was observed in the basic (pH = 8) range, which is due to better adsorption of the cationic CV dye over the catalyst surface (pH_{pzc} = 6.59, determined by pH drift method), which was not substantial under the acidic conditions. The degradation was monitored as a function of the CV concentration, Fig. 7(b),

which declines with the increase in its concentration. The increased concentration prevents the light from reaching the catalyst surface, in addition to the saturation of active catalytic sites available for the adsorption. The Ce-Bi₃YO₆/rGO dosage was optimized by loading the catalyst from 10–50 mg as displayed in Fig. 7(c), and the maximum degradation was observed at 40 mg of the catalyst dosage, after which no significant increase was observed. The coexisting ions include Sulphate, chloride, carbonate, bicarbonate, and nitrite. The chloride ions did not alter the rate of the degradation process, while the sulphate ions contributed to the minimum extent, and the carbonate, bicarbonate, and nitrite ions significantly dropped the CV degradation due to scavenging of the radical species that perform the degradation process.

The 1st-order kinetics model was applied to the experimental data of CV degradation to determine the photocatalytic kinetics in the presence of Bi₃YO₆, Ce-Bi₃YO₆, and Ce-Bi₃YO₆/rGO (Fig. 8(a–d)). The CV degradation follows 1st-order kinetics with corresponding rate constant values of 0.0315 min^{−1} (62.37%),

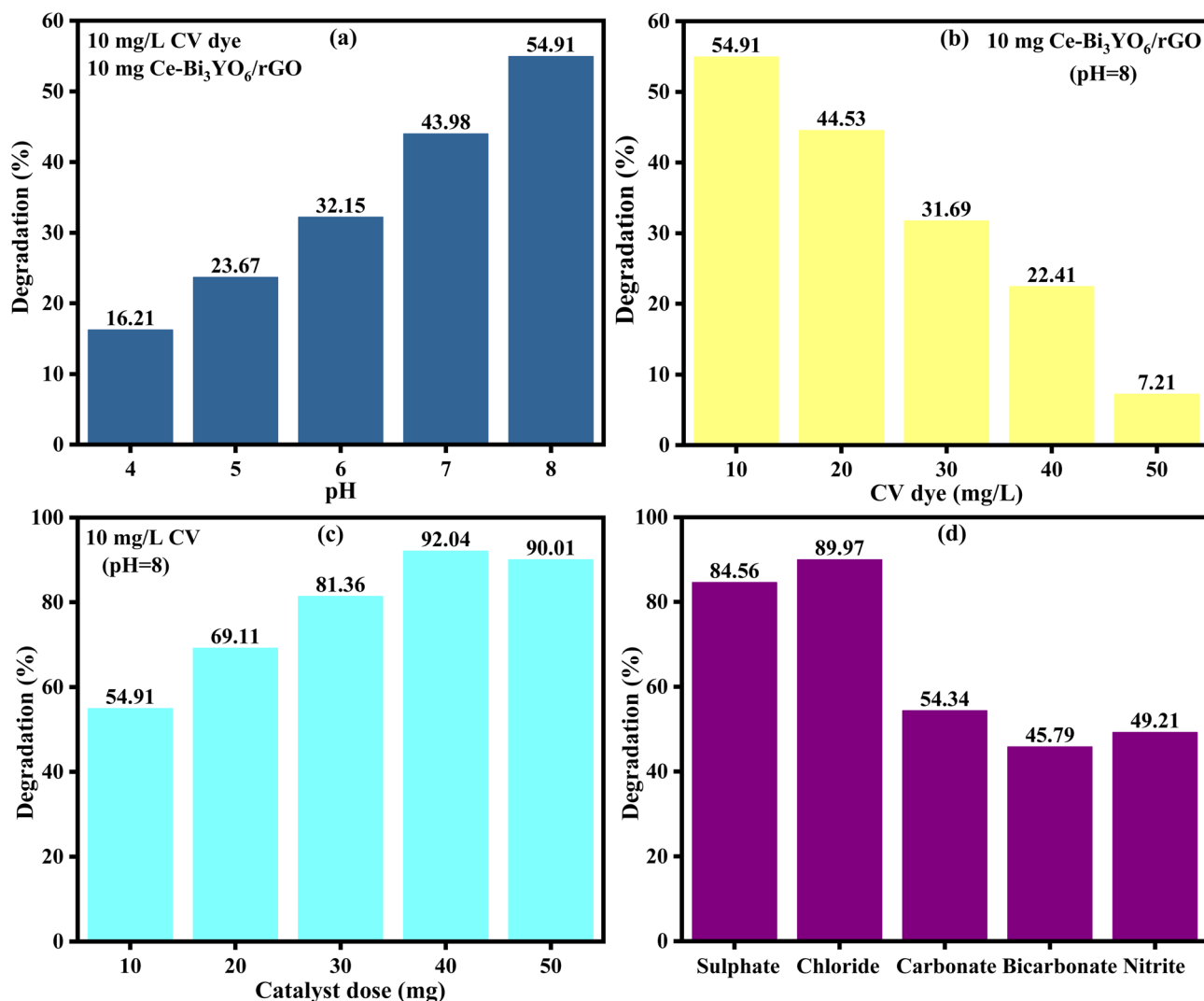


Fig. 7 Effect of pH (a), CV concentration (b), catalyst dose (c), and common coexisting ions (d) on the degradation of CV over the Ce-Bi₃YO₆/rGO.

0.0455 min⁻¹ (76.28%), and 0.0800 min⁻¹ (92.04%) in the presence of Bi₃YO₆, Ce-Bi₃YO₆, and Ce-Bi₃YO₆/rGO.

Scavenging test was applied to the CV degradation by the catalyst Ce-Bi₃YO₆/rGO under visible-light irradiation using AgNO₃, p-BQ, EDTA-2Na, and IPA as specific scavengers for quenching of photo-generated e⁻, [•]O₂⁻, h⁺, and HO[•] radicals, respectively (Fig. 9a).^{50,51} The extreme decline in CV degradation (33.55%) was observed in the IPA presence, which quenched the HO[•] radicals, revealing the substantial contribution of HO[•] in CV degradation. The AgNO₃ presence affected the CV degradation to a minimal extent (81.72%), which expresses the least contribution of e⁻ in the degradation process. In light of the scavenging results, the CV degradation was predominantly controlled by the HO[•] radicals, and the species contribution varies in accordance with (33.55%) HO[•] > (48.82%) [•]O₂⁻ > (67.56%) h⁺ > (81.72%) e⁻ to the overall CV degradation. The reusability of the photocatalyst is conspicuous, not only for economic purposes but also for environmental stability. The Ce-Bi₃YO₆/rGO was reused for five cycles to probe its stability

and efficacy (Fig. 9b). The CV degraded to 92.04%, 90.13%, 88.51%, 86.31%, and 84.22%, with minimal decline in degradation extent, which could be due to the recovery loss of the catalyst. The excellent reusability throws light on the stability of the catalyst for its substantial potential in sunlight-mediated photocatalytic wastewater treatment.

The photocatalytic degradation of CV over the Ce-Bi₃YO₆/rGO involves a synergistic mechanism driven by the structural and electronic framework of the designed composite (Fig. 9c). In light irradiation, the Ce-Bi₃YO₆ absorbs photons of visible light, exciting e⁻ from its valence band (VB) to the conduction band (CB), generating a positive h⁺ in VB.⁵² The electrons from the CB of Ce-Bi₃YO₆ are transported to the highly conductive rGO, which inhibits the rapid recombination of the h⁺-e⁻, which is substantial to start the redox reaction to generate active radical species.⁵³ The band potentials, *E*_{VB} and *E*_{CB}, were calculated by applying the relations, *E*_{VB} = *X* - *E*_e + 1/2(*E*_g) and *E*_{CB} = *E*_g - *E*_{VB},⁵⁴ where *E*_g = free electron energy (hydrogen scale), *E*_g = optical bandgap, and *X* = electronegativity.⁵⁵ For

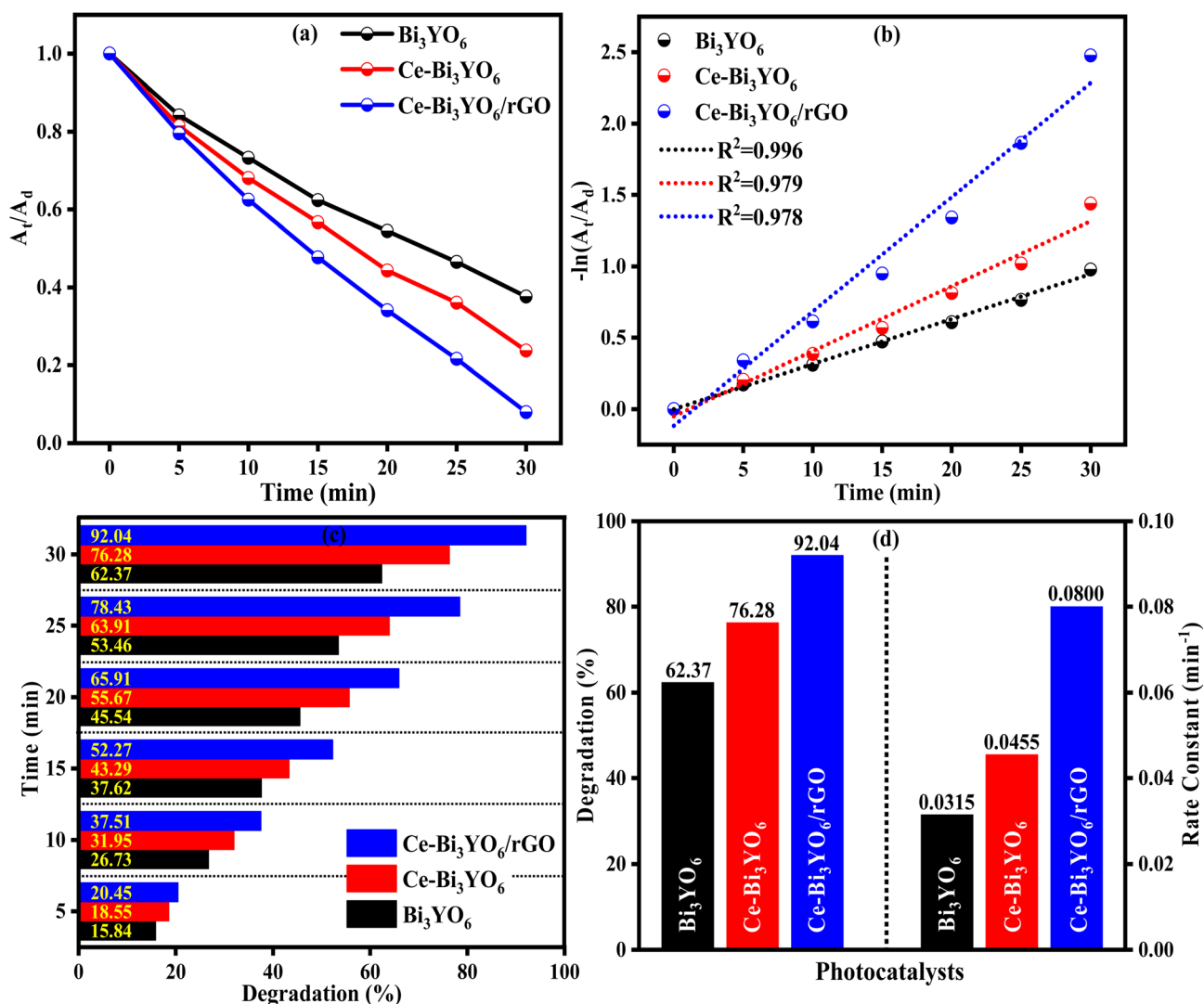


Fig. 8 Kinetics model fitting (a and b), comparison of CV degradation at specified time intervals (c), and overall CV degradation (%) achieved and rate constants for the catalysts Bi₃YO₆, Ce-Bi₃YO₆, and Ce-Bi₃YO₆/rGO (d).

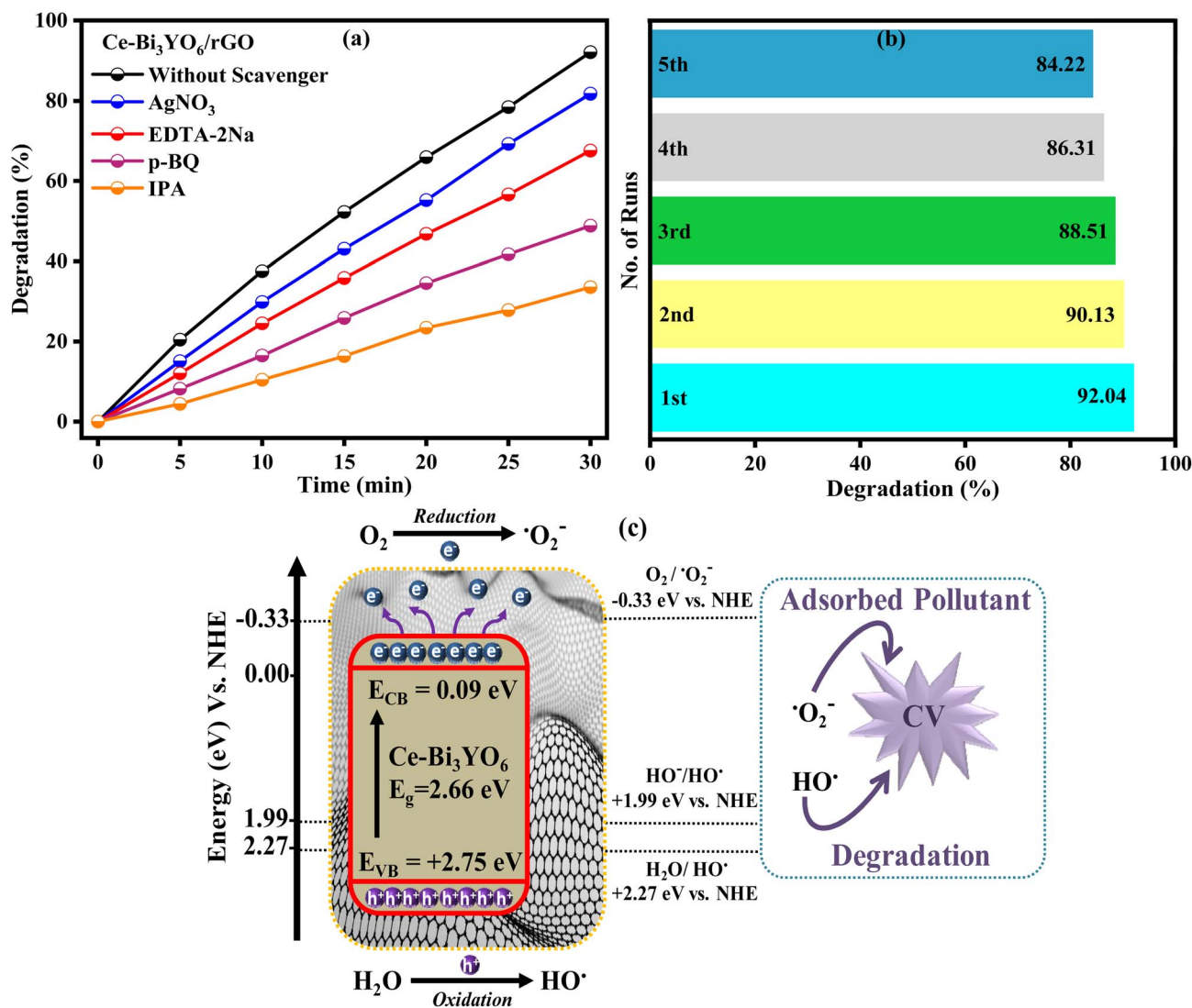


Fig. 9 CV degradation (%) with and without scavenger in the presence of Ce-Bi₃YO₆/rGO catalysts (a), reusability of the catalyst Ce-Bi₃YO₆/rGO (b), and schematic display of Ce-Bi₃YO₆/rGO photocatalyst for CV degradation (c).

Ce-Bi₃YO₆, the potentials were $E_{VB} = +2.75$ eV and $E_{CB} = 0.09$ eV. Thermodynamically, the $E_{VB} = +2.75$ eV can generate HO^\cdot radicals ($HO^-/HO^\cdot = 1.99$ eV and $H_2O/HO^\cdot = 2.23$ eV vs. NHE) but $E_{CB} = 0.09$ eV is unable for $\cdot O_2^-$ radicals generation ($O_2/\cdot O_2^- = -0.33$ eV vs. NHE).⁵⁶ The scavenging test demonstrated the $\cdot O_2^-$ involvement in CV degradation, which is not formed directly from the E_{CB} of the Ce-Bi₃YO₆ but indirectly from the electrons stored in the rGO component.^{57,58} The encapsulation of Ce-Bi₃YO₆ with rGO not only reduces the rapid h^+e^- recombination, but also the generation of radicals for the CV degradation.⁵⁹

The improved photocatalytic property of the Ce-Bi₃YO₆/rGO hybrid material can be ascribed to the synergetic effect between Ce-doping and rGO encapsulation. Ce ions incorporated into the lattice of Bi₃YO₆ create oxygen vacancies, which narrow bandgap and extend its absorption spectrum to visible light. Besides that, the role of rGO is also to provide a highly conductive scaffold for the photogenerated electrons to be

transferred at a high rate without undergoing charge recombination. Such a combined effect enhances the charge separation efficiency and greatly improves the photocatalytic degradation efficiency under visible light irradiation.

4. Conclusion

Synergistically modified Ce-Bi₃YO₆/rGO material has been designed to facilitate the charge separation and transportation to drive the redox reaction for photocatalytic performance under visible light. Initially, the pure Bi₃YO₆ and its Ce-doped composition, Ce-Bi₃YO₆, were fabricated by the hydrothermal route, followed by the encasing of Ce-Bi₃YO₆ flakes in rGO sheets by ultrasonication. XRD, FTIR, and TGA confirm the phase composition, crystal structure development, and thermal stability up to 400 °C. The SEM analysis exposed the 2D-like flakes of Ce-Bi₃YO₆ evenly encased in rGO covering. The PL and UV-vis spectroscopic studies revealed the extended visible light response of the modified material. The electrical



measurements and electrochemical findings demonstrate delayed recombination of the photogenerated h^+e^- pair. The Ce-doping decreases the E_g and increases the electronic excitation by absorbing photons from the visible light range; these photoexcited electrons from the CB of Ce-Bi₃YO₆ spatially transferred to the conductive framework of the rGO covering. The Ce-Bi₃YO₆/rGO exhibits substantial PC efficacy from the Ce-Bi₃YO₆ and Bi₃YO₆ for the CV degradation in aqueous media with 1st order reaction kinetics. The scavenging studies highlight the notable contribution of HO[•] radicals in CV degradation, and the reusability of Ce-Bi₃YO₆/rGO describes its stability and environmental stability. In light of the aforementioned findings, the designed Ce-Bi₃YO₆/rGO catalyst features promising photocatalytic efficacy for wastewater treatment.

Author contributions

(1) Muhammad Shahid: writing – original draft, methodology. (2) M. M. Rashed: funding acquisition, project administration, resources. (3) Mohamed Abdel Rafea: data curation, formal analysis. (4) Mohamed Ibrahim Attia: investigation, formal analysis. (5) Mohamed R. El-Aassar: visualization, data curation. (6) Abdullah K. Alanazi: writing – review & editing. (7) Imran Shakir: investigation, data curation. (8) Muhammad Aadil: formal analysis, supervision. (9) Mazen R. Alrahili: formal analysis, validation.

Conflicts of interest

There are no conflicts to declare.

Data availability

The datasets generated and analysed during this study are not publicly available due to [confidentiality/size limitations], but they can be obtained from the corresponding author upon reasonable request.

Acknowledgements

This work was supported and funded by the Deanship of Scientific Research at Imam Mohammad Ibn Saud Islamic University (IMSIU) (grant number IMSIU-DDRSP2502).

References

- 1 Y. Sari, P. L. Gareso, B. Armynah and D. Tahir, A review of TiO₂ photocatalyst for organic degradation and sustainable hydrogen energy production, *Int. J. Hydrogen Energy*, 2024, **55**, 984–996.
- 2 G. Anandhi and M. Iyapparaja, Photocatalytic degradation of drugs and dyes using a machine learning approach, *RSC Adv.*, 2024, **14**, 9003–9019.
- 3 M. Lyu, C. Wang, Y. Rong, J. Wei, Y. Yang, Y. Liu, G. Wei, Q. Zhang, C. Wang and J. Xiu, Advances in modification of Bi₂MoO₆ and its photocatalysis: a review, *J. Alloys Compd.*, 2024, **982**, 173759.
- 4 H. Zhou, H. Wang, C. Yue, L. He, H. Li, H. Zhang, S. Yang and T. Ma, Photocatalytic degradation by TiO₂-conjugated/coordination polymer heterojunction: Preparation, mechanisms, and prospects, *Appl. Catal. B Environ. Energy*, 2024, **344**, 123605.
- 5 Y. Zhu, Y. Feng, Y. Yan, Z. Wang, X. Zhang, S. Faraji, Q. Ai, T. Xie, X. Weng, L. Zhou, T. Zhai, Y. Liu, X. Huang, C.-y. Lin, S. Glass, B. Shin, Y. Han, A. A. Martí, P. M. Ajayan, M. Liu, Q. Li and J. Lou, Covalent organic framework/hexagonal boron nitride heterostructure photocatalysts for efficient degradation of emerging contaminants, *Mater. Today*, 2025, **91**, 253–260.
- 6 G. M. Subaiea, A. Rasheed, A. Alobaida, N. E. Khalifa, H. E. El-Horany, M. F. Warsi and A. A. Katamesh, Cerium-doped bismuth-oxy chloride microspheres encased in conductive carbon support with tuned visible-light activity and delayed charge carrier recombination for the degradation of organic compounds, *J. Water Proc. Eng.*, 2025, **77**, 108561.
- 7 M. H. Elsayed, M. Abdellah, A. Z. Alhakemy, I. M. Mekhemer, A. E. A. Aboubakr, B.-H. Chen, A. Sabbah, K.-H. Lin, W.-S. Chiu and S.-J. Lin, Overcoming small-bandgap charge recombination in visible and NIR-light-driven hydrogen evolution by engineering the polymer photocatalyst structure, *Nat. Commun.*, 2024, **15**, 707.
- 8 B. Fu, Y. Pan, P. Zhao, L. Zhang, J. Zhuo, J. Feng, B. Li, L. Yao, J. Xi and X. Lan, “Edge in-situ heterogeneous” BiOI based on defect engineering and non-noble metal deposition: Boosting visible-light photocatalytic sterilization, *Chem. Eng. J.*, 2024, **491**, 152071.
- 9 H. A. Alburaih, M. Aadil, S. R. Ejaz, W. Hassan, A. Anwar, S. Anjum, S. Aman, M. S. Al-Buriah, Z. A. Alrowaili and A. V. Trukhanov, Wet-chemical synthesis of urchin-like Co-doped CuO: A visible light trigger photocatalyst for water remediation and antimicrobial applications, *Ceram. Int.*, 2022, **48**, 21763–21772.
- 10 N. H. Hanh, Q. T. M. Nguyet, T. Van Chinh, L. D. Duong, T. X. Tien, L. Van Duy and N. D. Hoa, Enhanced photocatalytic efficiency of porous ZnO coral-like nanoplates for organic dye degradation, *RSC Adv.*, 2024, **14**, 14672–14679.
- 11 S. M. Albukhari, L. Al-Hajji and A. A. Ismail, Construction of nn heterojunction copper manganese spinel/mesoporous WO₃ photocatalyst for efficient H₂ evolution rate from aqueous glycerol, *Renewable Energy*, 2024, **228**, 120649.
- 12 S. H. Lisar and G. Karimi, Halloysite nanotubes (MHNTs) modified S-scheme g-C₃N₄/γ-Fe₂O₃ photocatalyst for enhancing charge separation and photocatalytic activity, *J. Alloys Compd.*, 2024, **977**, 173429.
- 13 A. K. Mourya, R. P. Singh, R. Belgamwar, V. Polshettiwar and A. V. Wankhade, Synergistic effect of dendritic fibrous nanosilica and In₂O₃ photocatalysts for enhanced visible-light-driven hydrogen generation, *Ind. Eng. Chem. Res.*, 2024, **63**, 17767–17777.
- 14 G. Shi, Y. Wu, W. Liu, Y. Hou, Q. Li and S. Luo, 2D/3D ZnS/SnO₂ photocatalyst with Z-scheme heterojunction for



- efficient degradation of organic pollutants, *Inorg. Chem. Commun.*, 2025, **178**, 114504.
- 15 M. Cheng, H. Li, Z. Wu, Z. Yu, X. Tao and L. Huang, Synergistic effects of CQDs and oxygen vacancies on CeO₂ photocatalyst for efficient photocatalytic nitrogen fixation, *Sep. Purif. Technol.*, 2025, **354**, 129299.
 - 16 K. P. Makhado, M. M. Mphahlele-Makgwane, N. Kumar, P. G. Baker and P. R. Makgwane, Current updates on p-type nickel oxide (NiO) based photocatalysts towards decontamination of organic pollutants from wastewater, *Mater. Today Sustain.*, 2024, **25**, 100664.
 - 17 Y. Yang, C. Flatebo, J. Liang, P. Dong, J. Yuan, T. Wang, J. Zhang, W. Chen, J. Wu, P. M. Ajayan, L. Ci, Q. Li and J. Lou, Towards methyl orange degradation by direct sunlight using coupled TiO₂ nanoparticles and carbonized cotton T-shirt, *Appl. Mater. Today*, 2016, **3**, 57–62.
 - 18 K. M. Katubi, A. Rasheed, A. Ihsan, B. Shaheen, Z. Alrowaili, M. Al-Buriah, M. I. Din, I. Shakir and S. Munir, Neodymium-doped nickel cobaltite reinforced with 2D MXene nanocomposite (Nd-NiCo₂O₄/MXene) for enhanced photocatalytic degradation of the organic pollutants, *Opt. Mater.*, 2024, **152**, 115390.
 - 19 A. Rasheed, I. Bibi, F. Majid, S. Kamal, B. Taj, M. Raza, N. Khaliq, K. M. Katubi, S. Ezzine and N. Alwadai, Mn doped SrFe₂O₁₉ fabricated via facile microemulsion route and solar-light-driven photocatalytic removal of crystal violet dye, *Phys. B*, 2022, **646**, 414303.
 - 20 K. Shafiq, M. Aadil, W. Hassan, Q. Choudhry, S. Gul, A. Rais, A. A. Fattah, K. H. Mahmoud and M. Z. Ansari, Cobalt and holmium co-doped nickel ferrite nanoparticles: synthesis, characterization and photocatalytic application studies, *Z. Phys. Chem.*, 2023, **237**, 1325–1344.
 - 21 M. Irshad, M. M. Ibrahim, S. Siddique, U. Younas, G. A. Mersal, S. S. Al-Juaid, A. Irshad and M. Farooq Warsi, Boosting the properties of Ag-decorated Ni₃V₂O₈ via 1D-CNTs integration for advanced photocatalytic and anti-bacterial performance, *Ceram. Int.*, 2025, **51**(14), 19704–19714.
 - 22 Q. Raza, G. Fatima, B. Lu, I. Bibi, J. An and S. Lim, In-situ synthesis and synergistic effect of Ag/Al@ SrFe₂O₁₉ decorated with graphitic carbon nitride: mechanistic insight of photocatalytic and antimicrobial susceptibility, *Surf. Interfaces*, 2025, 107203.
 - 23 A. M. Omar, A. H. Abdelhamid, H. S. Mohamed and G. Khabiri, An urchin-shaped hierarchical Bi₂S₃ ornamented with SnO₂ QDs nanocomposite as a multifunctional photocatalyst for water treatment, *J. Alloys Compd.*, 2025, **1038**, 182672.
 - 24 Y. Zhu, Y. Liu, Q. Ai, G. Gao, L. Yuan, Q. Fang, X. Tian, X. Zhang, E. Egap and P. M. Ajayan, In situ synthesis of lead-free halide perovskite-COF nanocomposites as photocatalysts for photoinduced polymerization in both organic and aqueous phases, *ACS Mater. Lett.*, 2022, **4**, 464–471.
 - 25 M. F. Abou Taleb and M. M. Ibrahim, Harnessing the potential of cube-like Holmium doped bismuth niobate (Ho-Bi₅Nb₃O₁₅) amalgamated with rGO sheets for rapid photocatalytic elimination of crystal violet and acetylsalicylic acid, *Ceram. Int.*, 2024, **50**, 31985–31997.
 - 26 A. Mandal and K. Kargupta, Cu-Doped 2D-Bi₂MoO₆ Nanoribbon/rGO Photocatalysts for Selective Ethanol Production by Photocatalytic CO₂ Reduction, *ACS Appl. Nano Mater.*, 2025, **8**, 3471–3486.
 - 27 Y. Zhu, H. Shen, Q. Ai, Y. Feng, B. Shin, M. Gonzales, Y. Yan, Z. He, X. Huang and X. Zhang, Double Layer SiO₂-Coated Water-Stable Halide Perovskite as a Promising Antimicrobial Photocatalyst under Visible Light, *Nano Lett.*, 2024, **24**, 13718–13726.
 - 28 Z. Ren, L. Yang, X. Tang, Q. Xu, Y. Niu, Y. Lv and M. Liu, Visible light-driven characterisation of AgI/CeO₂/rGO nanocomposites and their application in levofloxacin degradation, *J. Environ. Chem. Eng.*, 2024, **12**, 113124.
 - 29 M. Sabir, M. Ramzan, M. Imran, S. R. Ejaz, A. Anwar, S. Ahmad, M. Aamir and M. Aadil, Synthesis of La_{1-x}Gd_xFe_{1-y}Co_yO₃/r-GO nanocomposite with integrated features for the treatment of hazardous industrial effluents, *Ceram. Int.*, 2022, **48**, 9134–9145.
 - 30 M. Sajjad, S. U. Asif, L. Guan, Y. Jiao, Y. Jiang, L. Zhang, J. Wen, S. Zhang, Y. Lin and S. Zhang, Bismuth yttrium oxide (Bi₃YO₆), a new electrode material for asymmetric aqueous supercapacitors, *J. Inorg. Organomet. Polym. Mater.*, 2021, **31**, 1260–1270.
 - 31 Y. Li, Y. Liu, X. Liu and X. Li, Visible light-driven efficient degradation of Rhodamine B using rGO/Bi₂O₂CO₃/BiOCl composite photocatalysts, *Diamond Relat. Mater.*, 2024, **144**, 111038.
 - 32 S. R. Khaladkar, O. Maurya, G. Gund, B. Sinha, D. Dubal, R. Deshmukh and A. Kalekar, Extrinsic pseudocapacitive NiSe/rGO/g-C₃N₄ nanocomposite for high-performance hybrid supercapacitors, *ACS Appl. Mater. Interfaces*, 2024, **16**, 11408–11420.
 - 33 Y. Cai, J. Li, Q. Zhang, C. Liu, C. Wang, H. Shi, L. Jiang and D. Wu, Ambient ultrafast green synthesis of cyclodextrin-based metal-organic framework through solvent-induced in-situ crystallization for high-efficiency capture of radioactive iodine, *Sep. Purif. Technol.*, 2025, **376**, 134078.
 - 34 Y. Li, J. Bu, Y. Sun, Z. Huang, X. Zhu, S. Li, P. Chen, Y. Tang, G. He and S. Zhong, Efficient degradation of norfloxacin by synergistic activation of PMS with a three-dimensional electrocatalytic system based on Cu-MOF, *Sep. Purif. Technol.*, 2025, **356**, 129945.
 - 35 H. Qian, B. Yuan, Y. Liu, R. Zhu, C. Zhang and H. Li, Superhydrophobic Photochromic TiO₂/Bi₂WO₆ Materials Promote Photocatalytic CO₂ Reduction under Visible Light Irradiation, *ACS Appl. Mater. Interfaces*, 2025, **17**, 45649–45659.
 - 36 H. Somaily, Tailoring the electrical, optical, physical, and photocatalytic properties of indium-doped cerium molybdate microstructures reinforced with a 2D carbonaceous, *Ceram. Int.*, 2024, **50**, 36717–36730.
 - 37 Z. Liu, G. Wang, Y. Li, H. Li and N. Deng, Carboxymethyl-β-cyclodextrin functionalized TiO₂@ Fe₃O₄@ RGO magnetic photocatalyst for efficient photocatalytic degradation of



- tetracycline under visible light irradiation, *J. Environ. Chem. Eng.*, 2024, **12**, 113303.
- 38 S. Kumar, R. Ahlawat, G. Rani, J. Devi and A. Kamboj, In situ synthesis of RGO and CNT-templated diamond-shaped Fe-based metal-organic frameworks: Exploring their remarkable photocatalytic and antioxidant properties, *Inorg. Chem. Commun.*, 2025, **171**, 113589.
 - 39 H. Chai, J. Nan, W. Jin, F. Wu, B. Liu and Y. Guo, Zinc phthalocyanine/polymer carbon nitride S-scheme heterojunction with internal electric field and near-infrared absorption for photocatalytic H₂O₂ production, *Chem. Eng. J.*, 2024, **489**, 151293.
 - 40 G. Suresh, M. S. Meera, A. Anil, S. George and S. M. A. Shibli, Yeast Reduced Ti³⁺ Self-Doped SrTiO₃/rGO-In-Ni₂P Nanocomposite for Efficient Visible Light-Driven Hydrogen Generation, *ACS Appl. Nano Mater.*, 2024, **7**, 16806–16822.
 - 41 M. Rao, I. Bibi, F. Majid, S. Kamal, A. Kausar, H. Elhouichet, Q. Raza, G. Fatima, N. Alwadai and M. Iqbal, Exploring charge dynamics in CuO/Fe₂O₃-doped NiCo₂O₄/rGO nanocomposites for visible-light-driven photocatalysis, *Ceram. Int.*, 2025, **51**, 8231–8248.
 - 42 V. Harshitha and D. Suresh, Role of rGO reinforced Er-WO₃ in biological, photocatalytic, luminescence and forensic applications, *Phys. B*, 2025, 417518.
 - 43 A. Darmawan, D. A. B. Bara, M. Al Fahmi, H. Muhtar and D. N. Bima, Synergistic photodegradation of Remazol Black B dye using sulfur-doped g-C₃N₄/rGO composite: The dual role of thiourea, *J. Water Proc. Eng.*, 2025, **72**, 107545.
 - 44 M. Aldrery, M. Aadil, A. Khalid, M. R. Alrahili, M. Elhadi, F. Alresheedi, M. Algarni, M. R. El-Aassar and A. El Jery, Hydrothermally synthesized hierarchical Pom-Pom-like gadolinium modified tungsten oxide reinforced with rGO for annihilation of acetylsalicylic acid and crystal violet, *Surf. Interfaces*, 2024, **55**, 105396.
 - 45 H. Esfandian, M. R. Cherati and M. Khatirian, Electrochemical behavior and photocatalytic performance of chlorpyrifos pesticide decontamination using Ni-doped ZnO-TiO₂ nanocomposite, *Inorg. Chem. Commun.*, 2024, **159**, 111750.
 - 46 Q. Zhou, Z. Liu, X. Wang, Y. Li, X. Qin, L. Guo, L. Zhou and W. Xu, Co₃S₄-pyrolysis lotus fiber flexible textile as a hybrid electrocatalyst for overall water splitting, *J. Energy Chem.*, 2024, **89**, 336–344.
 - 47 A. Zulkiflee, M. M. Khan, M. Y. Khan, A. Khan and M. H. Harunsani, Nb₂O₅/BiOCl composite as a visible-light-active photocatalyst for the removal of RhB dye and photoelectrochemical studies, *J. Photochem. Photobiol. A*, 2024, **446**, 115177.
 - 48 S. Mysamy, T. Govindasamy and B. Subramanian, Systematic exploration of defect-rich 2D nanopetal assembled 3D ZnO nanoflowers for improved photocurrent generation and photocatalytic performance, *J. Environ. Chem. Eng.*, 2024, **12**, 111700.
 - 49 M. Haruna, F. Eshun, C. K. Bandoh, E. S. Agorku, O. Francis, N. K. Asare-Donkor and A. A. Adimado, Binary Ce-doped-ZnO/rGO composite as excellent photocatalyst for bromothymol blue dye degradation, *Sustain. Chem. Environ.*, 2024, **5**, 100069.
 - 50 N.-B. Trinh, T. A. Nguyen, S. Van Vu, H.-G. T. Vo, T. N. H. Lo, I. Park and K. Q. Vo, Modified hydrothermal method for synthesizing titanium dioxide-decorated multiwalled carbon nanotube nanocomposites for the solar-driven photocatalytic degradation of dyes, *RSC Adv.*, 2024, **14**, 34037–34050.
 - 51 Y. Lu, Y. Zhao, S. Wang and B. Hu, Exploring charge-transfer of 2D borophene in carbon nitride: boosting uranium photoreduction, *Desalination*, 2026, **619**, 119488.
 - 52 A. Kumawat, M. Rawat, N. S. Leel and N. Kumar, Enhancement of optical and surface electronic properties in rGO-CuO nanocomposites for improved photocatalytic activities, *Opt. Mater.*, 2025, 117103.
 - 53 T. M. Vo, T. M. H. Nguyen and C. W. Bark, Reduced graphene oxide-supported copper (I) oxide composites for the degradation of methylene blue: exploring the capacity of RGO as an electron capturer for achieving highly stable photocatalytic activity, *ACS Appl. Electron. Mater.*, 2024, **6**, 4391–4405.
 - 54 K. Vanasundari, P. Ponnarasi and G. Mahalakshmi, A green approach to synthesis of Ag-doped CeO₂ nanorods embedded reduced graphene oxide nanocomposite for excellent photocatalytic and antimicrobial activity, *Inorg. Chem. Commun.*, 2024, **165**, 112523.
 - 55 M. Ishfaq, M. Aadil, S. R. Ejaz, W. Hassan, N. M. Panduro-Tenazoa, M. E. El Sayed, M. N. Murshed and Z. M. El-Bahy, Synthesis of binary metal doped CeO₂ via the subcritical hydrothermal method for photo-mineralizing methyl orange dye, *J. Alloys Compd.*, 2023, **960**, 170661.
 - 56 Z. Zuo, W. Zhao, C. Shi, Y. Wang, D. Li, Q. Wu, H. Ge, P. Si and Y. Yang, Enhanced piezo-photocatalytic degradation of pharmaceutical antibiotics through band engineering, *J. Mater. Sci.: Mater. Electron.*, 2025, **36**, 1603.
 - 57 A. Rebekah, R. Maddipatla and K.-S. Lee, Visible light sensitive photocatalytic properties of Bi₂WO₆/Ag₂CO₃ heterojunction combined with reduced graphene oxide for the removal of organic dyes, *Mater. Res. Bull.*, 2025, **183**, 113175.
 - 58 A. Alazmi, Synergistic surface modification and metal doping in perovskites: A route to photocatalytic excellence, *Surf. Interfaces*, 2025, **73**, 107487.
 - 59 S. Noor, S. Sajjad, S. A. K. Leghari, Z. Yousaf and S. M. El-Bahy, Comparative role of Ag and Ce doping on WO₃ and GO modified nanostructures for bi-functional effective photocatalyst and electro catalyst, *J. Phys. Chem. Solids*, 2024, **193**, 112183.

